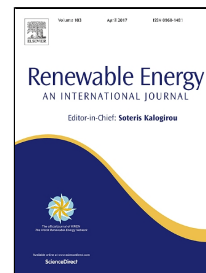


Accepted Manuscript

Performance Evaluation of Solar Air Heater With Novel Hyperbolic Rib Geometry

Deep Singh Thakur, Mohd. Kaleem Khan, Manabendra Pathak



PII: S0960-1481(16)31161-2
DOI: 10.1016/j.renene.2016.12.092
Reference: RENE 8429
To appear in: *Renewable Energy*
Received Date: 05 November 2015
Revised Date: 25 December 2016
Accepted Date: 29 December 2016

Please cite this article as: Deep Singh Thakur, Mohd. Kaleem Khan, Manabendra Pathak, Performance Evaluation of Solar Air Heater With Novel Hyperbolic Rib Geometry, *Renewable Energy* (2016), doi: 10.1016/j.renene.2016.12.092

This is a PDF file of an unedited manuscript that has been accepted for publication. As a service to our customers we are providing this early version of the manuscript. The manuscript will undergo copyediting, typesetting, and review of the resulting proof before it is published in its final form. Please note that during the production process errors may be discovered which could affect the content, and all legal disclaimers that apply to the journal pertain.

HIGHLIGHTS

- ❖ 2D CFD simulation of solar air heater
- ❖ Performance evaluation of novel hyperbolic rib
- ❖ Parametric study to evolve optimized hyperbolic rib profile
- ❖ Comparison with other rib geometries

PERFORMANCE EVALUATION OF SOLAR AIR HEATER WITH NOVEL HYPERBOLIC RIB GEOMETRY

Deep Singh Thakur

Mohd. Kaleem Khan¹

Manabendra Pathak

Department of Mechanical Engineering, Indian Institute of Technology Patna, Patna
(INDIA)

ABSTRACT

This paper presents 2D CFD analysis for the evaluation of thermo-hydraulic performance of artificially roughened solar air heater's absorber plate with novel hyperbolic ribs using ANSYS FLUENT 15.0. The motivation for the present study is derived from the fact that formation of eddies across a rib do influence thermo-hydraulic performance of a flat plate solar air heater. The design of hyperbolic ribs is such that it prevents entrapment of eddies facilitating higher heat transfer rate leading to superior thermos-hydraulic performance. The developed model has been validated for smooth (duct without artificial roughness) as well as roughened ducts. The rib profile parameters have been optimized by performing simulation runs by varying roughness height (e) from 0.5 mm to 2 mm and pitch (P) from 10 mm to 20 mm. The optimum performance is achieved for $e = 1$ mm and $P = 10$ mm at $Re = 6000$. The performance of this novel rib is compared with rectangular, triangular and semicircular rib geometries and is found to be the best among all up to $Re = 10000$.

Keywords: Flat plate solar air heater; Artificial roughness; Thermo-hydraulic performance; CFD simulation

¹ Corresponding author: Tel.: +91-612-2552019, Fax: +91-612-2277383, Email: mkkhan@iitp.ac.in

1 Nomenclature

2	c_p	Specific heat (J/kg-K)
3	H	Duct height (m)
4	L	length (m)
5	p	pressure (Pa)
6	P	pitch (m)
7	q''	heat flux (W/m ²)
8	Q_u	Energy gain by air (W)
9	T	Temperature (°C)
10	W	Duct width (mm)

11 Greek Letters

12	α	Attack angle
13	ϕ	Wedge angle
14	η	Thermo-hydraulic performance
15	μ	Viscosity N-s/m ²

16 Subscript

17	i	inlet value
18	o	outlet values
19	m	arithmetic mean of inlet and outlet value
20	f	roughened surface
21	s	smooth surface
22	w	absorber wall

23 ABBREVIATIONS

- 1 RNG Re-normalized group
 2 SAH Solar air heater

3

4 **1. Introduction**

5 With depleting fossil fuel resources, the world is looking at unconventional energy resources
 6 such as wind, tidal, solar, geothermal etc. Among these unconventional energy resources solar
 7 energy is abundant and cheap. Direct conversion of solar energy to electricity using solar
 8 photovoltaic cells is marred by poor conversion efficiency and high cost. Solar thermal
 9 technology, on the other hand, involves conversion of solar energy into useful thermal energy,
 10 which is a low cost solution to some practical problems such as drying, sterilization, space
 11 heating etc. Solar air heaters utilize solar energy to heat air, which in turn, can be used to serve
 12 various purposes. Mainly they are used for drying of food grains and timber.

13 In order to improve the thermo-hydraulic performance of solar air heaters, numerous efforts
 14 have been made by the researchers worldwide [1-11]. A detailed review of works related to
 15 performance enhancement of solar collectors has recently been carried out by our group [12]. In
 16 general, artificial roughness is created on the absorber plate to increase surface area and
 17 turbulence near its surface which in turn enhances heat transfer rate. However, this increase in
 18 heat transfer rate is at the cost of increase in frictional pressure drop across the collector. Thus, to
 19 evaluate the performance of a solar air heater, a thermo-hydraulic performance parameter is
 20 defined by the following relation [13]:

$$21 \quad \eta = \frac{Nu_f / Nu_s}{(f_f / f_s)^{1/3}} \quad (1)$$

where, Nu is the Nusselt number, f is the Darcy's friction factor and subscripts f and s represents frictional and smooth surfaces respectively. This parameter compares the heat transfer of artificially roughened duct to that of smooth duct under constant pumping power condition [9]. Better performance entails higher value of thermo-hydraulic performance parameter η .

Artificial roughness on absorber plate is generally obtained by employing ribs on its surface. Table 1 presents the summary of important studies pertaining to heat transfer enhancement of solar air heaters using rib geometries.

A comprehensive review of literature has revealed that use of various rib geometries, rib height, pitch and their arrangement (inline or staggered) on the absorber plate affects heat transfer and pressure drop characteristics significantly. Several researchers [14-16] have concluded on the basis of their 2D CFD analyses that the performance of rectangular ribs is far better than other rib geometries such as semi-circular, circular and triangular. It has also been established that eddies formed across a rib do influence thermo-hydraulic performance of a flat plate solar air heater. In rectangular and triangular geometries eddies get entrapped in upstream and downstream corners leading to the formation of local hotspots, which finally results in reduced heat transfer rate. With this in mind, a novel design of hyperbolic rib with parabolic tip has been evolved, which not only eliminates the entrapment of eddies to a greater extent but also results in better thermo-hydraulic performance. A 2D CFD analysis has been performed on this novel rib geometry and compared its performance with other rib geometries. In addition, a parametric study has also been carried out to optimize rib height and pitch. Further, a comparison of thermo-hydraulic performance of proposed rib design has also been made with rectangular, triangular and semi-circular geometries.

2. Mathematical Modeling and Solution Methodology

The flow domain of solar air heater used in the present CFD simulation is shown in Fig. 1(a). It consists of an aluminum absorber plate of length L_2 , which is subjected to constant heat flux conditions. The entrance length L_1 and exit length L_3 have been provided on either side of absorber plate. The purpose of providing entrance length is to allow the flow to develop fully before it comes in contact with absorber plate. Further, exit length allows proper mixing of cold and hot air streams. In Fig. 1(b), plate thickness is shown just to relate the present simulation work with the real ribbed absorber plate.

As per ASHRAE Standard 93 GA30329, following are the correlations for entrance and exit lengths [17]:

$$L_1 = 5\sqrt{WH} \quad (2)$$

$$L_3 = 2.5\sqrt{WH} \quad (3)$$

where W and H are width and height of the channel respectively.

Values of geometrical and operating parameters are listed in Table 2.

The present CFD code is based on the following assumptions:

- Air flow is two-dimensional, steady and fully developed turbulent.
- Absorber plate (smooth or roughened) is thin and as such conduction losses can be neglected.
- Only flow domain is discretized to obtain the simulation results.
- Thermo-physical properties of air are assumed constant.
- Radiation heat losses are negligible.

Governing Equations

The governing equations for steady flow of air through the duct are obtained by applying laws of conservation of mass, momentum and energy.

Mass conservation or continuity equation

$$\frac{\partial}{\partial x_j}(u_j) = 0 \quad (4)$$

Momentum conservation or Navier-Stokes equation

$$\frac{\partial(\rho u_i u_j)}{\partial x_j} = -\frac{\partial p}{\partial x_i} + \mu \frac{\partial}{\partial x_j} \left(\frac{\partial u_i}{\partial x_j} + \frac{\partial u_j}{\partial x_i} \right) + \frac{\partial(-\rho \overline{u_i' u_j'})}{\partial x_j} \quad (5)$$

Energy conservation equation

$$\frac{\partial(u_j T)}{\partial x_j} = \alpha \frac{\partial}{\partial x_j} \left(\frac{\partial T}{\partial x_j} \right) + \frac{\mu_t}{\rho \sigma_t} \frac{\partial}{\partial x_j} \left(\frac{\partial T}{\partial x_j} \right) \quad (6)$$

Boundary Conditions

Equations (4-6) have been solved with the help of following boundary conditions

- Inlet

$$u = 1.75-7.88 \text{ m/s}, v = 0 \text{ m/s}, T = 300 \text{ K}, \text{ Turbulent intensity} = 5\%$$

- Absorber plate wall

$$u = v = 0 \text{ m/s (no-slip)}, q'' = 1000 \text{ W/m}^2 \text{ (constant heat flux)}$$

- Other walls

$$u = v = 0 \text{ m/s (no-slip)}, q'' = 0 \text{ W/m}^2 \text{ (insulated)}$$

- Outlet

$$p = p_{\text{atm}}, \text{ Backflow turbulent intensity} = 5\%$$

where u and v are the velocity components in x and y directions respectively.

Numerical Methodology

Computations are performed using finite volume based ANSYS FLUENT 15.0 CFD code.

Steady pressure based solver is used to solve the governing equations in a sequential manner.

The momentum and energy equations have been discretized with second order upwind scheme.

The coupling of pressure with velocity is done with the help of SIMPLE (Semi Implicit Pressure Linked Equation) algorithm. Convergence criteria are: sum of residual mass should be less than 10^{-6} and sum of residual energy should be less than 10^{-9} . The structured quadrilateral elements in a non-uniform grid have been used, where grid is clustered near the walls. A layout of the grid is shown in Fig. 2(a) and Fig. 2(b) for smooth duct and artificially roughened duct with proposed hyperbolic ribs (for $e = 1.0$ mm and $P = 10$ mm), respectively. The respective results of grid independency tests are shown in Fig. 2(c) and Fig. 2(d), which are the plots of Nu versus Re . The grids are made finer by increasing the number of elements from 20176 to 313243 for smooth duct and from 27658 to 345239 for the roughened duct. The deviation in Nu is less than 0.1 percent between the consecutive grid sizes, is the criteria for grid independency.

In addition, the adaptive mesh is used in simulation of each rib geometry and further refinement is done at every 40 iterations interval. This ensures the correct mesh resolution and makes simulation results reliable and dependable. Table 3 shows the final mesh size for each and every configuration of roughened duct with proposed hyperbolic rib geometry.

It should be noted that the present study has been undertaken for turbulent flow ($4000 < Re < 15000$) in the duct. In the present simulation, RNG $k-\epsilon$ turbulent model has been used as it predicts the best results compared to other available turbulent models (SST and $k-\omega$ models) [18]. The turbulence kinetic energy (k) and turbulence specific dissipation rate (ϵ) are solved from their respective transport equation.

$$\frac{\partial(\rho k)}{\partial t} + \frac{\partial(\rho k u_i)}{\partial x_i} = \frac{\partial}{\partial x_j} \left[\frac{\mu_t}{\sigma_k} \frac{\partial k}{\partial x_j} \right] + 2\mu_t E_{ij} E_{ij} - \rho \epsilon \quad (7)$$

$$\frac{\partial(\rho \epsilon)}{\partial t} + \frac{\partial(\rho \epsilon u_i)}{\partial x_i} = \frac{\partial}{\partial x_j} \left[\frac{\mu_t}{\sigma_\epsilon} \frac{\partial \epsilon}{\partial x_j} \right] + C_{1\epsilon} \frac{\epsilon}{k} 2\mu_t E_{ij} E_{ij} - C_{2\epsilon} \rho \frac{\epsilon^2}{k} \quad (8)$$

In above, $C_\mu = 0.09$, $\sigma_k = 1.00$, $\sigma_\varepsilon = 1.30$, $C_{1\varepsilon} = 1.44$ and $C_{2\varepsilon} = 1.92$. Subscript k and ε represent the turbulence kinetic energy and turbulence specific dissipation rate. The eddy viscosity (μ_t) is expressed in terms of turbulence kinetic energy (k) and turbulence specific dissipation rate (ε) as follows:

$$\mu_t = \rho C_\mu \frac{k^2}{\varepsilon} \quad (9)$$

To capture the laminar sublayer region near the wall in the simulation, RNG k- ε model with enhanced wall treatment is employed. According to it, non-dimensionalized first layer thickness should be approximately equal to unity, i.e. $y^+ \approx 1$. The non-dimensionalized first layer thickness is defined as [19]

$$y^+ = \frac{y}{\nu/u_\tau} \quad \Rightarrow \quad y^+ = \frac{y}{\nu/\sqrt{\tau_w/\rho}} \quad (10)$$

where, y is the first layer thickness, ν is kinematic viscosity, ρ is fluid density and τ_w is the wall shear stress.

3. Results and Discussion

In this section, heat transfer and pressure drop characteristics of solar air heaters with different rib geometries are presented. However, validation of the proposed model is done for smooth duct (absorber plate without artificial roughness). Heat transfer and pressure drop characteristics are obtained by evaluating Nusselt number and friction factor for the flow inside the duct. Using the temperature data obtained from CFD simulation, the average heat transfer coefficient h is computed by applying energy balance:

$$Q_u = \dot{m} c_p (T_o - T_i) = hA(T_w - T_m) \quad (11)$$

Where T_i is inlet fluid temperature

T_o is outlet fluid temperature

T_w is the average wall temperature,

T_m is mean fluid temperature (arithmetic mean of T_i and T_o)

The average Nusselt number is given by

$$Nu = \frac{hD_h}{k} \quad (12)$$

In order to evaluate friction, pressure data (inlet and outlet of duct) from the CFD model is extracted and Darcy-Weisbach equation is used to evaluate Darcy friction factor f , i.e.

$$\Delta p_f = f \frac{L}{D_h} \left(\frac{1}{2} \rho V^2 \right) \quad (13)$$

where V is average fluid velocity inside the duct

Δp_f is difference between inlet and outlet fluid pressure

The proposed CFD model is validated with the following well-established smooth duct correlations:

Dittus-Boelter Nusselt number correlation [20] for heat transfer:

$$Nu = 0.023 Re^{0.8} Pr^{0.4} \quad (14)$$

Blasius friction factor correlation [20] for frictional pressure drop:

$$f = 0.316 Re^{-0.25} \quad (16)$$

A comparison of computed Nusselt number and Dittus-Boelter Nusselt number is shown in Fig. 3(a) whereas Fig. 3(b) compares computed friction factor with Blasius friction factor. It can be seen from Fig. 3 that there is an excellent agreement between the computed and theoretical results for both Nusselt number and friction factor. The mean percentage deviation for Nusselt number and friction factor are 2.94 % and 1.59 % respectively.

In addition to the above, the code has also been validated with the existing models for artificially roughened solar air heater ducts in Fig. 4. In fact, Fig. 4(a) shows a comparison between the present model and Chaube et al.'s [14] model for semi-circular ribs with $P/e = 13.33$ and $e = 3$ mm whereas present model is compared with Yadav and Bhagoria's [15] for triangular rib (equilateral) with $P/e = 10$ and $e = 1$ mm in Fig. 4(b). It can be seen that the present model has an excellent agreement with both the models. The mean percentage deviation is 2.67% with Chaube et al.'s [14] results and 1.74% with Yadav and Bhagoria's [15] results.

The performance of proposed novel hyperbolic rib with parabolic tip geometry is investigated by varying rib height e from 0.5 mm to 2 mm and pitch P from 10 mm to 20 mm. The performance is presented by means of three plots f versus Re , Nu versus Re and η versus Re . This parametric investigation is shown in Figs. 5-10. Moreover, the results of smooth duct are also plotted for the sake of comparison.

Effect of pitch and rib height on friction factor for different Re is shown in Fig. 5 and Fig. 6. In general, irrespective of roughness height and pitch, friction factor decreases with the increase in Re . There exists an inverse relation between f and Re (which is in line with Blasius equation and Moody's chart). Fig. 5 shows the variation of friction factor with pitch for different rib heights. It should be noted that at higher Re , the rate of fall in friction factor reduces and as such f versus Re plot tends to become flat. Compared to smooth duct, the f versus Re curves for roughened duct are steeper. For a given Re and rib height, increase in pitch causes a reduction in friction factor. This is due to the fact that increase in pitch causes a reduction in number of ribs on absorber plate resulting in less obstruction in the flow.

Variation of friction factor with rib height for different pitches is shown in Fig. 6. Clearly, the effect of roughness height on friction factor is more pronounced as compared to that of pitch. For a given Re and pitch, with the increase in roughness height friction factor increases due to eddies formation in the separated region on the downstream side of each rib (i.e. wake). Consequently, a pressure loss occurs across each rib due to incomplete pressure recovery at rear side of rib. This results in an increased overall frictional pressure drop (or friction factor) for a roughened duct. It can be seen from the figure that there is an appreciable increase in friction factor as rib height is increased from zero (smooth) to 0.5 mm. For rib height from 0.5 mm to 1.0 mm and from 1.0 mm to 1.5 mm, the rise in friction factor is not so high whereas from 1.5 mm to 2 mm rib height, again there is a substantial increase in friction factor.

Effect of pitch and rib height on Nusselt number for different Re is shown in Fig. 7 and Fig. 8. Fig. 7 shows the variation of Nusselt number with pitch for different rib heights. It is known that irrespective of Re convective heat transfer coefficient is significantly higher in roughened duct as compared with smooth duct. This fact is also evident from the figure and is due to the flow separation and mixing induced by eddies formation in the wake region of each rib. With the increase in pitch, there is a reduction in Nusselt number as mixing zones decrease due to the reduction in number of ribs for a given absorber plate length.

In Fig. 8 for any Re and pitch, heat transfer coefficient (or Nusselt number) increases with rib height. The difference in the values of Nu is more prominent for higher values of Re (as indicated by diverging curves). It should be noted that effect roughness height on heat transfer rate is significant beyond $Re = 6000$. This may be due to disturbances created are damped out in lower turbulent regime.

It is seen in the above discussion both friction factor and Nusselt number increase with the increase in roughness height and decrease in pitch. Heat transfer rate is being enhanced at the expense of increase pumping power (which is equal to the product of volume flow rate and frictional pressure drop). In order to find out the suitability of the proposed roughness geometry, the performance of a duct is evaluated using thermo-hydraulic performance parameter already defined in Eq. (1), which relates heat transfer rate with frictional pressure drop.

Fig. 9 and Fig. 10 show the effect of pitch and roughness height on thermo-hydraulic performance parameter, respectively. First there is an increase in thermo-hydraulic performance with increase in Re until it attains maximum value and then there is deterioration in the performance. The increase in η is associated with the dominance of heat transfer effects over the frictional effects whereas drop in η is due to the dominance of latter.. In Fig. 9, η decreases with the increase in pitch for any rib height. In fact with pitch approaching infinity, it would resemble the case of smooth plate. With the increase in pitch, the performance deteriorates as both heat transfer and pressure drop decrease. The reduction in Nusselt number is significantly higher than the reduction in friction factor.

In Fig. 10, with increase in rib height, the pattern is not as clear as it is in case of varying pitch (Fig. 9). For any pitch, the rib height $e = 2$ mm gives the worst performance whereas $e = 0.5$ mm rib shows the best performance for $P = 20$ mm. However, $e = 1$ mm rib shows a consistently higher performance for any pitch. The best thermo-hydraulic performance is achieved for roughness height $e = 1$ mm, pitch $P = 10$ mm at $Re = 6000$.

Flow patterns in the inter rib regions affect heat transfer mechanism significantly [1]. As the flow stream passes over the rib, flow could not follow the body contour and separates due to adverse pressure gradient resulting in the formation of eddies in the immediate downstream of

rib. However, flow reattaches the surface after a particular distance. It is the reattachment length which controls the heat transfer rate from the absorber plate surface. If pitch is small, the reattachment will not take place and there will be eddies entrapped between inter rib regions causing the surface temperature to increase locally. For effective heat transfer from the ribbed surface, the inter rib distance (pitch) should be sufficiently large so that flow gets reattached and flow inside the eddy starts interacting with the mainstream flow. Consequently, the local heat transfer coefficient is maximum at the point of reattachment. Entrapment of eddies anywhere (downstream as well as upstream side of rib) on the absorber plate causes a deterioration of heat transfer rate. A local rise in plate temperature adjacent to entrapped eddy is a sign of low value of local heat transfer coefficient. Fig. 11 shows temperature contours for two adjacent hyperbolic ribs for optimum conditions (i.e., $e = 1$ mm, $P = 10$ mm and $Re = 6000$). It can be clearly seen at the upstream side of rib, there is no local rise in temperature. This is due to the design of hyperbolic rib geometry, which does not allow eddies to form at the upstream side of rib. However, a hotspot (as indicated by red color) can be seen in the downstream side of rib. This may be due to fluid elements being at the eye of the eddy (adjacent to hotspot) could not come out easily leading to low heat dissipation. It is also evident with the velocity vector of the region shown in the inset.

Fig. 12 shows variation of local heat transfer coefficient and velocity gradient (or wall shear stress) along absorber plate length. From the basics of boundary layer theory, it is known that $du/dy = 0$ indicates the point of separation (reattachment or detachment). Thus, attachment and detachment of boundary layer at the rib surface can be determined by the sign of velocity gradient. Boundary layer is attached when $du/dy > 0$ and for $du/dy < 0$ it is detached (i.e. flow separation). In the present investigation, it should be remembered that ribs are downward facing

and therefore the sign of du/dy would be opposite for flow reversal. Variation of both heat transfer coefficient and velocity gradient have been purposely shown to identify the role of flow patterns on the heat transfer coefficient. Heat transfer coefficient is a function of flow velocity. Higher the flow velocity higher will be the heat transfer coefficient. In the first half of the rib velocity increases at the expense of pressure energy and as such heat transfer coefficient has increased whereas on the other half velocity gets reduced and there is reduction in heat transfer coefficient. In the inter-rib spacing, local heat transfer coefficient is governed by two different mechanisms: (a) the region under the eddy (separated flow) prior to reattachment (b) smooth duct behavior after reattachment. Eddies formation is desirable for convective heat transfer point of view simply because the fluid particles in motion near the surface will carry away heat from the surface.

However, entrapped eddies have an opposite effect as the same fluid elements will be in touch with heated surface and as such the temperature will rise locally leading to poor heat transfer rate. With reattachment of flow, the thermally boundary layer reappears and heat transfer coefficient varies inversely with distance in the direction of flow (as per Dittus-Boelter equation). Thus, heat transfer coefficient attains local maxima at reattachment point and it decreases because of smooth duct behavior. Further it can be seen that heat transfer pattern gradually stabilizes in flow direction as we move beyond the middle of absorber plate. Similar behaviors were also reported by Wang and Sunden [21] for different rib geometries

In Fig. 13, the performance of optimized hyperbolic rib geometry is compared with that of other conventional rib geometries such as rectangular, triangular and semicircular for $e = 1$ mm and $P = 10$ mm. Fig. 13(a) shows a comparison of friction factor with Re . Semi-circular geometry offers least pressure drop whereas rectangular geometry has the maximum pressure

drop. The proposed hyperbolic geometry also offers low frictional pressure drop close to that of semi-circular geometry. In Fig. 13(b), a comparison of Nusselt number for hyperbolic rib with all the above geometries has been presented. Semi-circular geometry behaves poorly compared to all other rib geometries. On the other hand, the proposed hyperbolic rib geometry is best in low Reynolds number range (4000-6000) whereas rectangular geometry offers the maximum Nusselt in high Reynolds number range (8000 and above). Thermo-hydraulic performance of each rib geometry is shown in Fig. 13(c). The proposed hyperbolic has fairly good thermo-hydraulic performance compared to other geometries. In fact, it is the best in the range $4000 < Re < 10000$. Among all rib geometries semi-circular geometry has the worst performance. Rectangular rib profiles are best suited for high Re applications.

4. Concluding Remarks and Future Scope

It is a well known fact that flow turbulence near the ribbed heated surface plays an important role in enhancing the thermohydraulic performance of a solar air heater. The rib geometry and its configuration (pitch and height) significantly influence the rate of heat removal from the surface. In the present work, a 2D CFD simulation was performed to investigate the effect of Reynolds number, roughness height and pitch on thermohydraulic performance of the roughened absorber plate for a novel hyperbolic rib geometry with parabolic tip. The performance of the proposed hyperbolic rib has been compared with other conventional rib geometries such as rectangular, triangular and semicircular. The code has been validated for both smooth and roughened ducts and is found to be in excellent agreement with the available literature. The optimum rib performance has been found to be achieved at roughness height $e = 1$ mm, pitch $P = 10$ mm and $Re = 6000$. The reason for optimized performance can be attributed to the fact that at this height

and pitch, entrapment of eddies between the consecutive ribs is avoided and sufficient space is available for the reattachment of the boundary layer. The condition is conducive for higher heat transfer rate from the heated surface. Further, it has been found that the thermo-hydraulic performance of the proposed rib geometry is superior to rectangular, triangular and semi-circular geometries for Re up to 10000. The proposed novel rib geometry avoids entrapment of small eddies in the corners at upstream and downstream sides, leading to an increase in heat transfer rate and reduction in friction factor. In other geometries because of the presence of sharp corners, eddies get entrapped resulting in the formation of hot spots underneath. However, at very high Reynolds number, heat transfer rate in rectangular ribs is more pronounced than the pressure drop effect causing an overall increase in its thermohydraulic performance.

For proper understanding of thermohydraulic performance of the proposed rib geometry in a real situation, the experimental and 3D numerical simulation is currently in the advanced stage at our research lab.

References

- [1] B.N. Prasad, J.S. Saini, Effect of artificial roughness on heat transfer and friction factor in a solar air heater, *Solar Energy*, 41 (1988), pp. 555–560
- [2] V. S. Hans, R.P. Saini, J.S. Saini, Performance of artificially roughened solar air heaters—A review, *Renew. Sustain. Energy Rev.*, 13(2009), pp 1854–1869
- [3] A. Saxena, Varun, A.A. Sebaii, A thermodynamic review of solar air heaters, *Renew. Sustain. Energy Rev.*, 43 (2015), pp. 863–890
- [4] S. kumar, R.P. Saini, CFD based performance analysis of a solar air heater duct provided with artificial roughness, *Renewable Energy*, 34 (2009), pp. 1285-1291

- 1 [5] B.N. Prasad, J.S. Saini, Optimal thermo-hydraulic performance of artificial roughened
2 solar air heater, *Solar Energy*, 47 (2) (1991), pp. 91–96
- 3 [6] S.K. Verma, B.N. Prasad, Investigation for optimal thermohydraulic performance of
4 artificially roughened solar air heaters, *Renewable Energy*, 20 (2000), pp. 19–36
- 5 [7] J.L. Bhagoria, J.S. Saini, S.C. Solanki, Heat transfer coefficient and friction factor
6 correlations for rectangular solar air heater duct having transverse wedge shaped rib
7 roughness on the absorber plate, *Renewable Energy*, 25 (2002), pp. 341–369
- 8 [8] M.K. Mittal, Varun, R.P. Saini, S.K. Singhal, Effective efficiency of solar air heaters
9 having different types of roughness elements on the absorber plate, *Energy*, 32 (2007),
10 pp. 739–745.
- 11 [9] S. Yadav, J.L. Bhagoria. A CFD (computational fluid dynamics) based heat transfer and
12 fluid flow analysis of a solar air heater provided with circular transverse wire rib
13 roughness on the absorber plate. *Energy*, 55(2013), pp.1127-1142
- 14 [10] T. Alam, R.P. Saini, J.S. Saini, Use of turbulators for heat transfer augmentation in an air
15 duct – a review, *Renewable Energy*, 62 (2014), pp. 689–715
- 16 [11] K. Yakut, N. Alemdaroglu, B. Sahin, C. Celik, Optimum design-parameters of a heat
17 exchanger having hexagonal fins, *Applied Energy*, 83 (2006), pp. 82–98
- 18 [12] S.Suman, M. K. Khan, M. Pathak, Performance enhancement of solar collectors—A
19 review, *Renew. Sustain. Energy rev.*, 49(2015), pp 192-210
- 20 [13] R.L. Webb, E.R.G. Eckert, Application of rough surface to heat exchanger design,
21 *IJHMT*, 15 (9) (1972), pp. 1647–1658

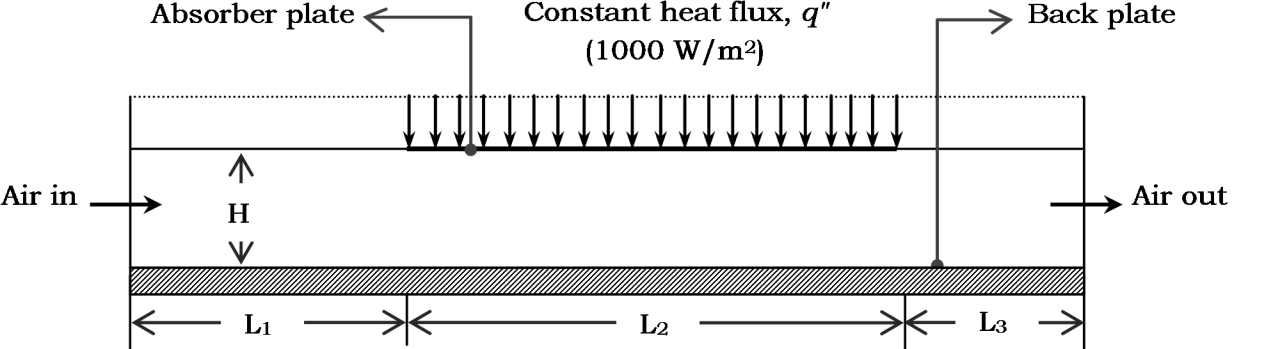
- [14] A. Chaube, P.K. Sahoo, S.C. Solanki, Analysis of heat transfer augmentation and flow characteristics due to rib roughness over absorber plate of a solar air heater. *Renewable Energy*, 31(2006), pp.317–331.
- [15] S. Yadav, J.L. Bhagoria. A CFD based thermo-hydraulic performance analysis of an artificially roughened solar air heater having equilateral triangular sectioned rib roughness on the absorber plate, *IJHMT*, 70(2014), pp.1016-1039
- [16] A.R. Jaurker, J.S. Saini, B.K. Gandhi. Heat transfer and friction characteristics of rectangular solar air heater duct using rib-grooved artificial roughness, *Solar Energy*, 80 (2006), pp. 895–907.
- [17] American Society of Heating, Refrigerating and Air Conditioning Engineers. ASHRAE Standard 93 GA30329 Method of testing to determine the thermal performance of solar collectors. Atlanta: ASHRAE, 2003.
- [18] S. Yadav, J.L. Bhagoria, Heat transfer and fluid flow analysis of solar air heater: A review of CFD approach, *Renew. Sustain. Energy Rev.*, 23 (2013), pp 60-79.
- [19] ANSYS 12.0 User's Guide, ANSYS Inc. April 2009
- [20] W.H. McAdams, *Heat Transmission*, McGraw-Hill, New York (1942)
- [21] L. Wang, B. Sunden, Experimental investigation of local heat transfer in a square duct with various-shaped ribs, *Heat and Mass Transfer*, 43 (2007), pp. 759–766

1

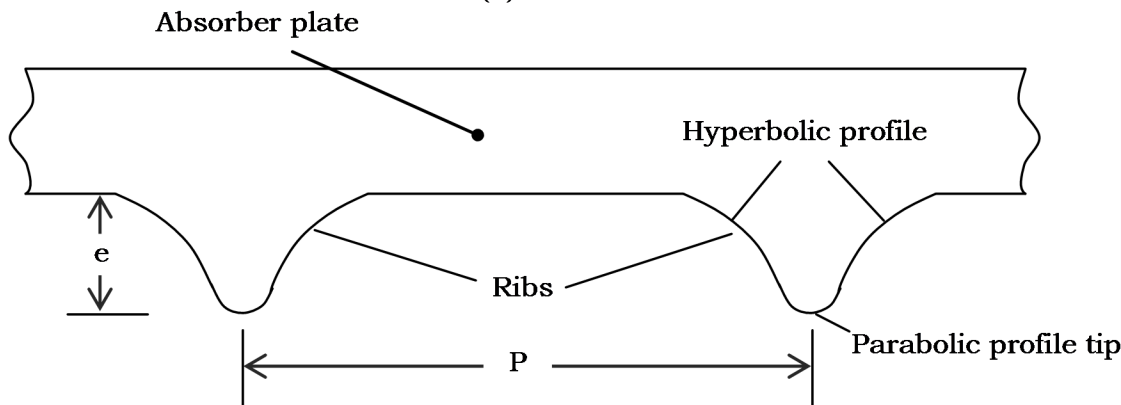
Figures and tables captions

Figure captions	
Fig. 1	Schematic diagram (a) solar air heater (b) section of absorber plate
Fig. 2	(a) Grid of quadrilateral elements (b) grid independency results
Fig. 3	Validation with smooth duct models (a) Dittus-Boelter correlation (b) Blasius equation
Fig. 4	Validation with roughened duct models (a) Chaube et al. [14] (b) Yadav and Bhagoria [15]
Fig. 5	f versus Re for different pitch at (a) $e = 2.0$ mm, (b) $e = 1.5$ mm, (c) $e = 1.0$ mm, (d) $e = 0.5$ mm
Fig. 6	f versus Re for different rib heights at (a) $P = 10$ mm, (b) $P = 15$ mm, (c) $P = 20$ mm
Fig. 7	Nu versus Re for different pitch at (a) $e = 2.0$ mm, (b) $e = 1.5$ mm, (c) $e = 1.0$ mm, (d) $e = 0.5$ mm
Fig. 8	Nu versus Re for different rib heights at (a) $P = 10$ mm, (b) $P = 15$ mm, (c) $P = 20$ mm
Fig. 9	η versus Re for different pitch at (a) $e = 2.0$ mm, (b) $e = 1.5$ mm, (c) $e = 1.0$ mm, (d) $e = 0.5$ mm
Fig. 10	η versus Re for different rib heights at (a) $P = 10$ mm, (b) $P = 15$ mm, (c) $P = 20$ mm
Fig. 11	Temperature contours of air inside the duct
Fig. 12	Variation of local heat transfer coefficient and velocity gradient along absorber plate
Fig. 13	Performance comparison (a) f versus Re (b) Nu versus Re (c) η versus Re
Table Captions	
Table 1	Summary of relevant literature
Table 2	Geometrical and operating parameters
Table 3	Final grid size for roughened duct with hyperbolic ribs of various configurations

2

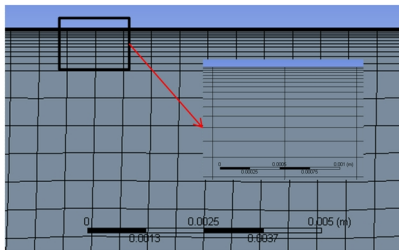


(a)

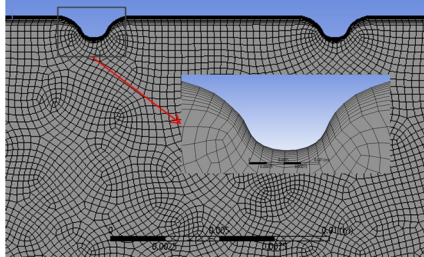


(b)

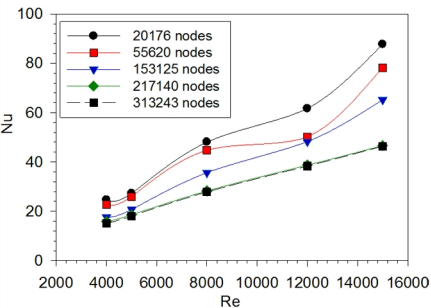
Fig. 1 Schematic diagram (a) solar air heater (b) section of absorber plate



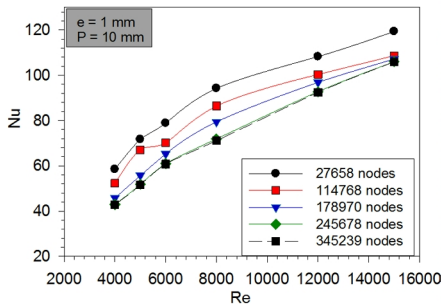
(a)



(b)

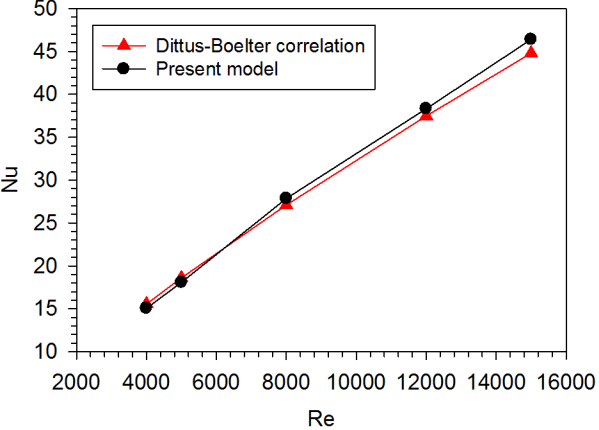


(c)

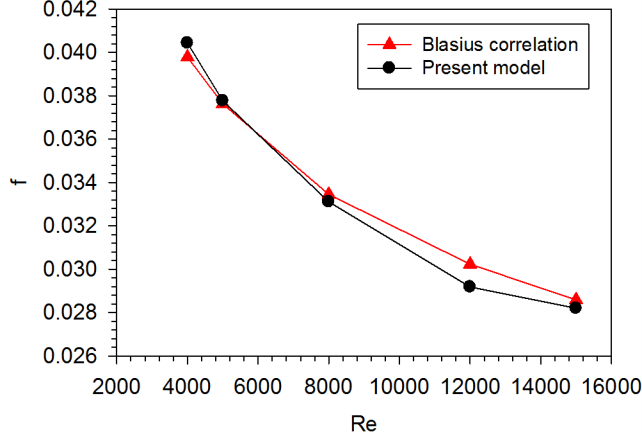


(d)

Fig. 2 Meshed domains (a) smooth duct (b) roughened duct and grid independency results for (c) smooth duct (d) roughened duct with hyperbolic ribs

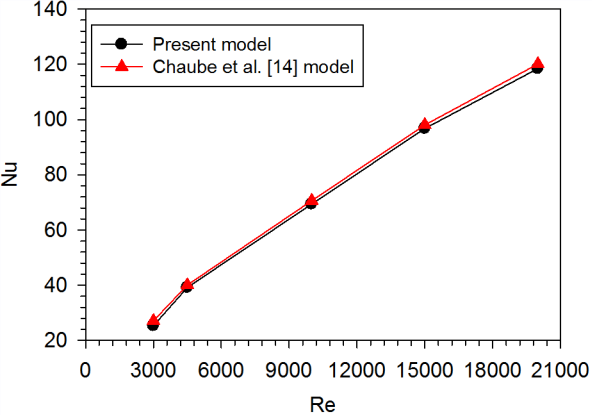


(a)

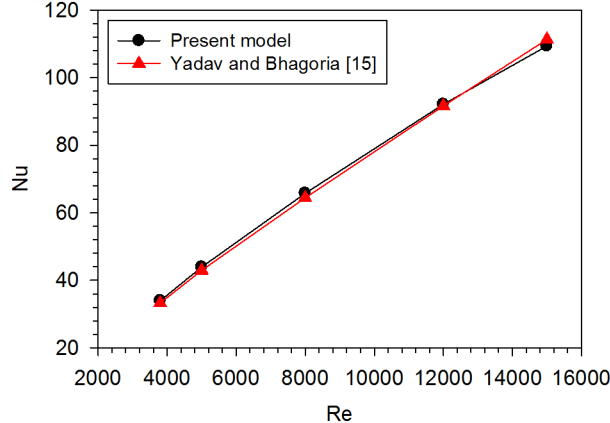


(b)

Fig. 3 Validation with smooth duct models (a) Dittus-Boelter correlation (b) Blasius correlation



(a)



(b)

Fig. 4 Validation with roughened duct models (a) Chaube et al.[14] (b) Yadav and Bhagoria[15]

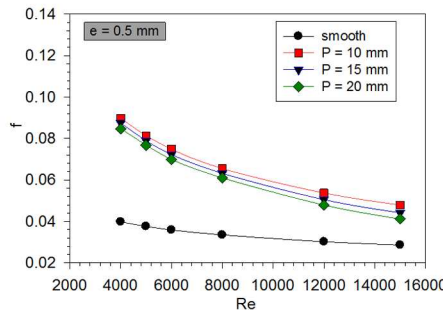
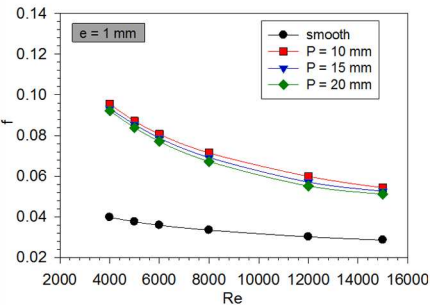
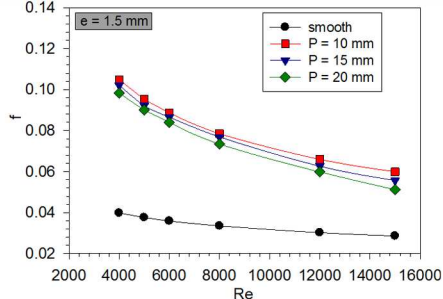
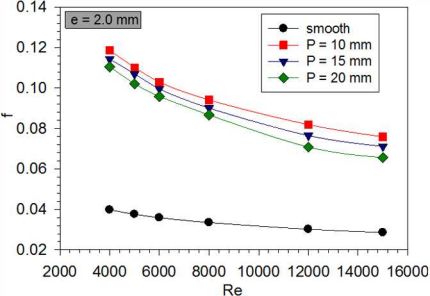


Fig. 5 f versus Re graph for varying pitch at constant rib height (a) $e = 2.0$ mm, (b) $e = 1.5$ mm, (c) $e = 1.0$ mm, (d) $e = 0.5$ mm

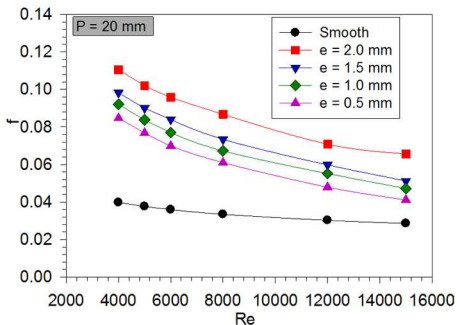
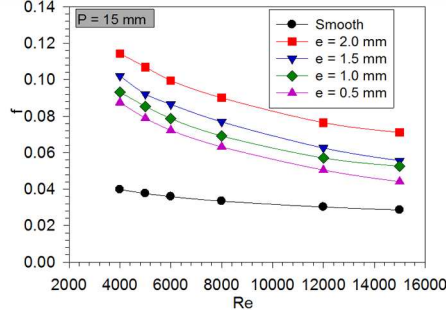
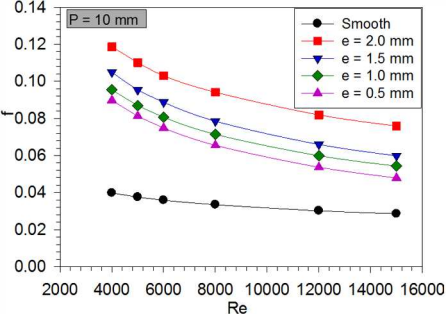


Fig. 6 f versus Re graph for varying rib height at constant pitch (a) $P = 10$ mm, (b) $P = 15$ mm, (c) $P = 20$ mm

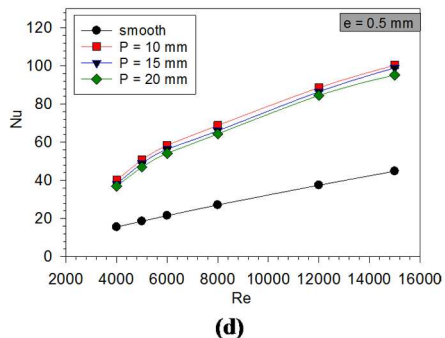
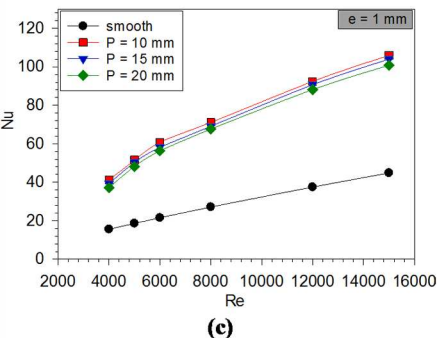
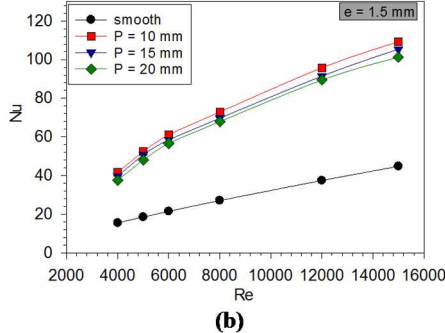
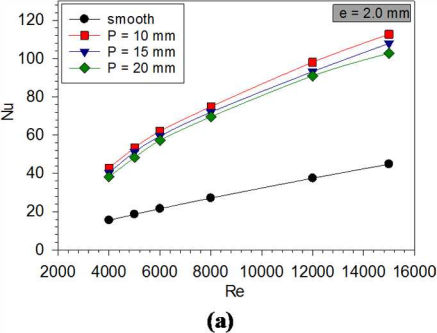
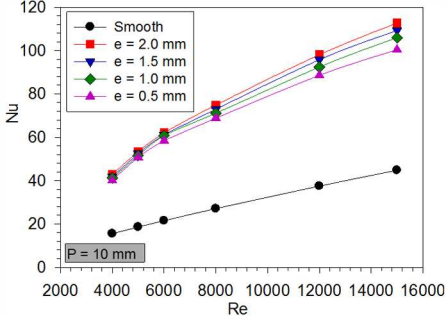
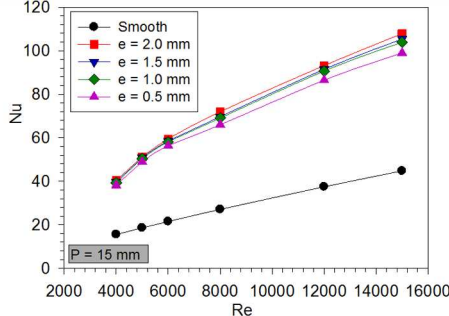


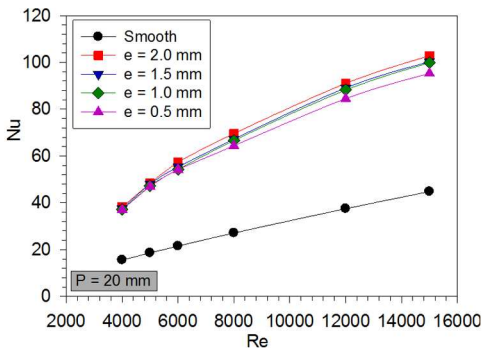
Fig. 7 Nu versus Re graph for varying pitch at constant rib height (a) $e = 2.0$ mm, (b) $e = 1.5$ mm, (c) $e = 1.0$ mm, (d) $e = 0.5$ mm



(a)



(b)



(c)

Fig. 8 Nu versus Re graph for varying rib height at constant pitch (a) $P = 10$ mm, (b) $P = 15$ mm, (c) $P = 20$ mm

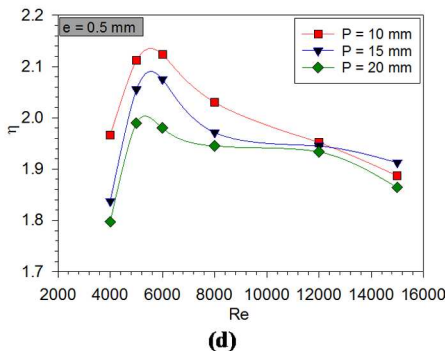
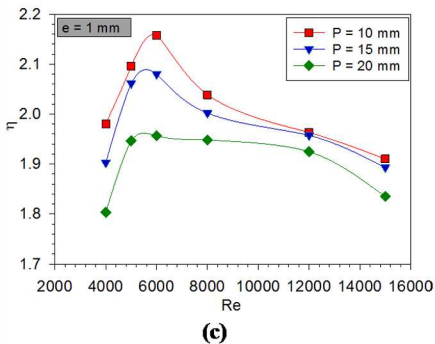
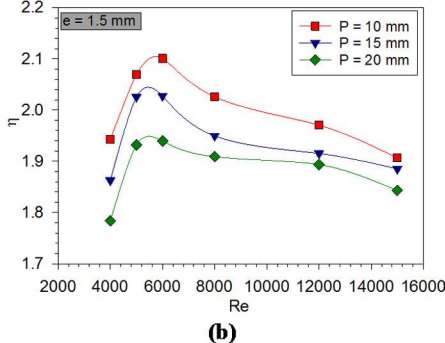
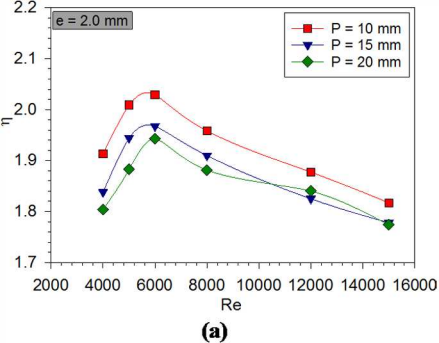


Fig. 9 η versus Re graph for varying pitch at constant rib height (a) $e = 2.0$ mm, (b) $e = 1.5$ mm, (c) $e = 1.0$ mm, (d) $e = 0.5$ mm

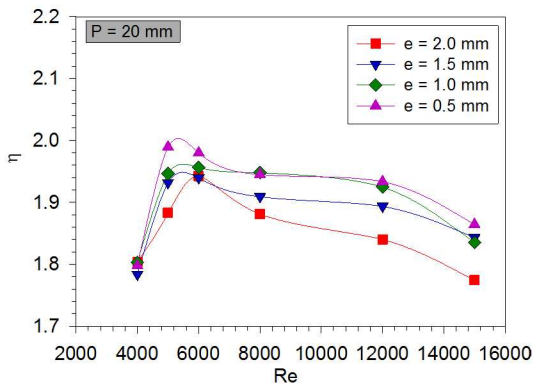
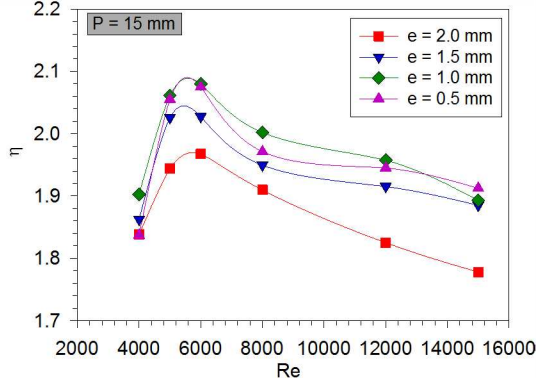
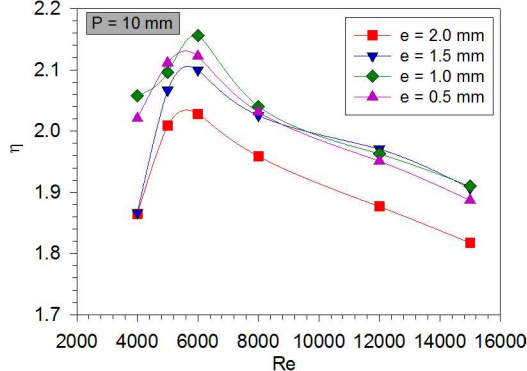


Fig. 10 η versus Re graph for varying rib height at constant pitch (a) $P = 10 \text{ mm}$, (b) $P = 15 \text{ mm}$, (c) $P = 20 \text{ mm}$

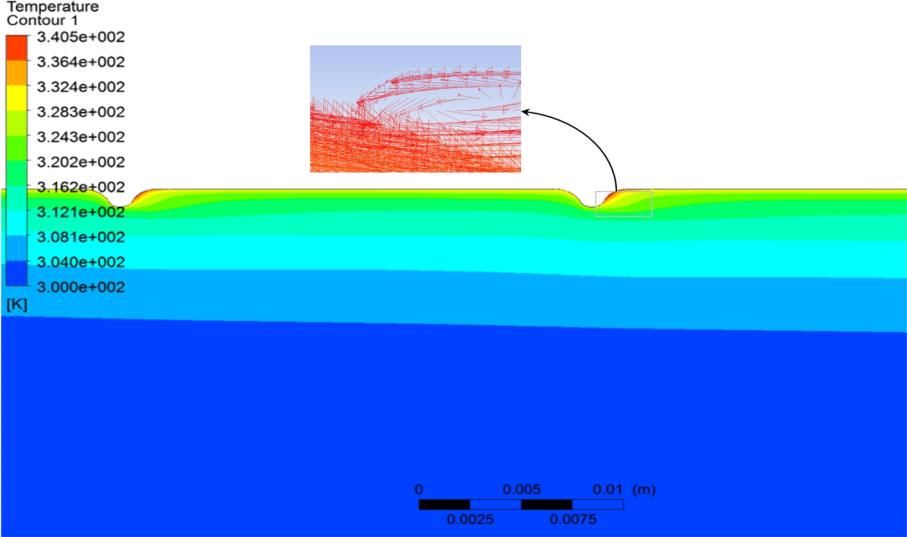
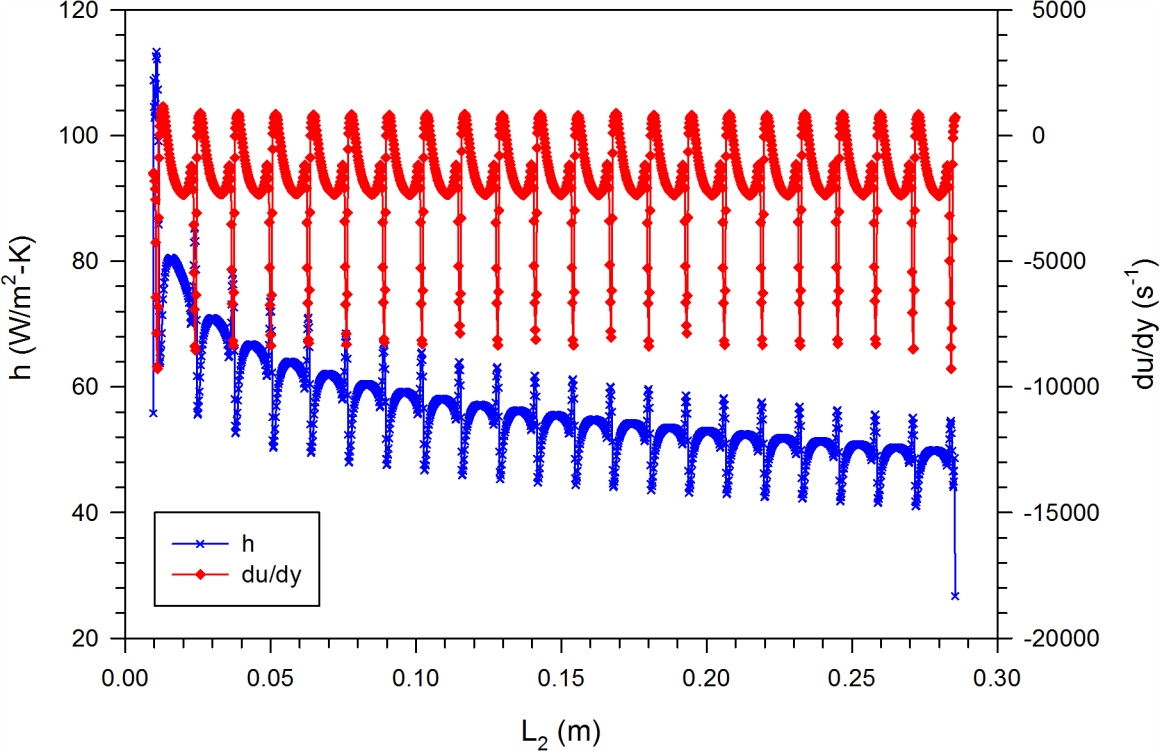
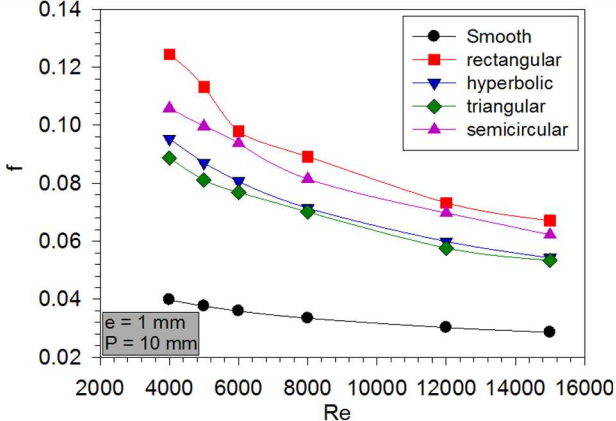
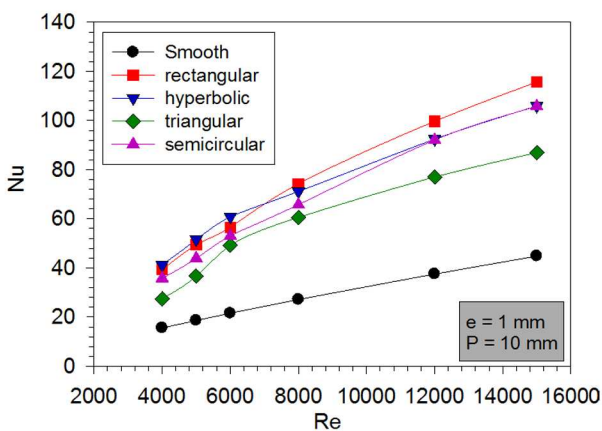


Fig .11 Temperature contour of air inside the duct

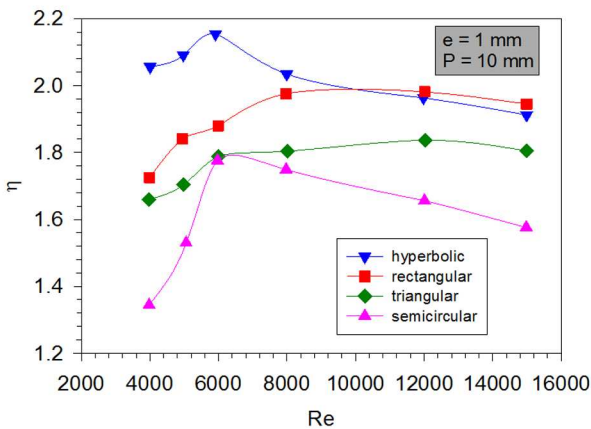




(a)



(b)



(c)

Fig. 13 Performance comparison (a) f versus Re (b) Nu versus Re (c) η versus Re

Table 1: Summary of relevant literature

Author(s) (year)	Rib Geometry	Analysis	Parameters	Findings
Prasad and Saini (1988)[1]	Circular transverse wire rib	Experimental	Re= 5000-50000 $e/D_h=0.02-0.033$ $P/e=10-20$	Maximum thermohydraulic performance is 1.66
Verma and Prasad (2000) [6]	Circular transverse wire rib	Experimental	Re= 5000-20000 $e/D_h=0.01-0.03$ $P/e=10-40$	Maximum thermohydraulic performance is 1.71
Bhagoria et al. (2002)[7]	Wedge	2D CFD analysis (no secondary flow)	Re = 3000 - 18000 $e/D_h = 0.015-0.033$ $P/e = 60.17 \phi^{-1.0264} - 12.12$ $\phi = 8^\circ - 15^\circ$	Maximum heat transfer at $P/e=7.57$, $\phi=10^\circ$ With increase in wedge angle ϕ also increases
Chaube et al (2006) [14]	Rectangular, Square, chamfered, semi-circular, circular	2D CFD analysis (no secondary flow)	Re=3000 - 20000	In all tested geometry rectangular give best thermohydraulic performance
Jaurker et al. (2006) [16]	Rectangular rib with grooves in absorber plate	Experimental	Re= 3000-21000 $e/D_h = 0.0181-0.0363$ $P/e = 4.5-10.0$ Groove position to pitch ratio 0.3-0.7	Maximum heat transfer and frictional pressure drop occur at $P/e=6$
Kumar and Saini (2009) [4]	Arc shaped wire	3D CFD analysis (secondary flow)	Re= 6000-18000 $e/D_h=0.0299-0.0426$ $\alpha / 90 = 0.33-0.66$	Maximum overall enhancement was 1.7
Yadav and Bhagoria (2013) [9]	Circular transverse wire rib	2D CFD (no secondary flow)	Re= 3800-18000 $e/D_h=0.021-0.042$ $P/e=7.14-35.71$	Maximum thermohydraulic performance is 1.65
Yadav and Bhagoria (2014) [15]	Equilateral triangle	2D CFD (no secondary flow)	Re= 3800-18000 $e/D_h=0.021-0.042$ $P/e=7.14-35.71$	Optimum $P/e=7.14$, $e/D_h = 0.042$

Table 2 Geometrical and operating parameters

<i>Geometrical parameters</i>		
Geometric parameter	Symbol	Value
Entrance length of duct, mm	L_1	225
Absorber plate length, mm	L_2	275
Exit length of duct, mm	L_3	121
Width of duct, mm	W	100
Depth of duct, mm	H	20
Hydraulic diameter, mm	D_h	33.33
<i>Operating parameters</i>		
Location	Boundary condition	Value
Inlet	Velocity inlet	1.72- 7.88 m/s
Outlet	Pressure outlet (gauge)	0
Absorber plate	Constant heat flux	1000 W/m ²
Other walls	Insulated	-

Table 3 Final grid size for roughened duct with hyperbolic ribs of various configurations

Configurations	Final Mesh Size
e = 0.5 mm, P = 10 mm	340173
e = 0.5 mm, P = 15 mm	338857
e = 0.5 mm, P = 20 mm	338021
e = 1.0 mm, P = 10 mm	345239
e = 1.0 mm, P = 15 mm	343734
e = 1.0 mm, P = 20 mm	342180
e = 1.5 mm, P = 10 mm	344756
e = 1.5 mm, P = 15 mm	343432
e = 1.5 mm, P = 20 mm	342196
e = 2.0 mm, P = 10 mm	344979
e = 2.0 mm, P = 15 mm	343188
e = 2.0 mm, P = 20 mm	342564